J. Fluid Mech. (2005), *vol.* 528, *pp.* 355–377.
doi:10.1017/S0022112004002939 Printed in the United Kingdom

Turbulence characteristics of two-dimensional channel flow with system rotation

By KOICHI NAKABAYASHI[1] AND OSAMI KITOH[2]

[1]Aichi University of Technology, 50-2 Manori, Nishihazama-cho, Gamagori-city, Aichi Prefecture 443-0047, Japan

[2]Nagoya Institute of Technology, Gokiso-cho, Showa-ku, Nagoya 466-8555, Japan

(Received 26 August 2003 and in revised form 13 October 2004)

Turbulence quantities have been measured for a low-Reynolds-number fully developed two-dimensional channel flow subjected to system rotation. Turbulence intensities, Reynolds shear stress, correlation coefficient, skewness and flatness factors, four-quadrant analysis, autocorrelation coefficient and power spectra are investigated. According to the dimensional analysis, the relevant parameters of this flow are the Reynolds number $Re^* = u^* D/\nu$ and the Coriolis parameter $Rc = \Omega\nu/u^{*2}$ for the wall region, and Re^* and $\Omega D/u^*$ for the turbulent core-region. The existence of a Coriolis region where turbulence intensities are defined by a new variable $y_c^* = y/\delta_c$ has been clarified on the pressure side in the rotating channel flow. The amount of turbulent kinetic energy transported by the Coriolis term is extremely small compared to the production term in the transport equation of Reynolds normal stress. However, the Coriolis term makes a large contribution to Reynolds shear stress transport on the pressure side of the channel. It is caused by the strong ejection which occurs periodically on the pressure side even though the ejection frequency is low. The strong ejection is conjectured to be caused by a large-scale longitudinal structure like a roll cell on the pressure side of the channel.

1. Introduction

Turbulent flow in a channel rotating around an axis perpendicular to its axis can be seen in cooling passages of gas turbine blades, electric motors and so on. Such rotating turbulent flows are influenced by the Coriolis force. Coriolis force effects are attributed to the induction of secondary flow by the endwall effect if there is a mean vorticity component perpendicular to the rotation axis and the promoting/suppressing effects on turbulence. If we confine consideration to channels having an aspect ratio larger than 4 and consider only the mid-plane of the channel, the secondary flow caused by the endwall effect does not appear, and the flow can be seen as nominally two-dimensional. In rotating two-dimensional flow, on the other hand, it is well known that roll cells occur above the critical value of a rotation parameter (Lezius & Johnston 1976). Pioneering work by Johnston, Haleen & Lezius (1972) on the fully developed turbulent flow through a duct of aspect ratio 7 demonstrated the following three Coriolis effects related stability phenomena: (i) the reduction (increase) of the turbulent wall-layer streak bursting rate in locally stabilized (destabilized) layers; (ii) the total suppression of turbulence production in the locally stabilized layer; and (iii) the development of roll cells on the destabilized side of the channel. An appropriate local stability parameter is shown to be the Richardson number, which

was introduced by Bradshaw (1969) for rotating flow by analogy with stratified flow.

For fully developed rotating channel flow, large-eddy simulations by Miyake & Kajishima (1986) and second-moment closure calculations by Launder, Tselepidakis & Younis (1987) and Shima (1993) have been reported. Recently, Kristoffersen & Andersson (1993) performed direct numerical simulations (DNS). We have studied the relation between the similarity laws of velocity profiles and the Coriolis force together with Reynolds number effects in low-Reynolds-number fully developed two-dimensional channel flow (Nakabayashi & Kitoh 1996), where consideration of turbulence was not reported.

Concerning turbulence quantities in turbulent boundary layers with system rotation, Koyama *et al.* (1979) and Watmuff, Witt & Joubert (1985) studied experimentally the relation between turbulence characteristics and the Coriolis force. The former indicated that the turbulent activities are weakened on the suction side of the channel (cyclonic case), whereas they are augmented on the pressure side (anti-cyclonic case). The latter authors clarified that the turbulence quantities follow an inner and outer scaling independent of rotation. Energy spectra of the streamwise velocity component indicated that, for a given non-dimensional distance, it was the low-wavenumber spectral components that were affected by rotation. Watmuff *et al.* observed Görtler-type vortices which corresponded to large spatially periodic spanwise variations of skin friction in the destabilized layers. Few other experimental result on the turbulence measurements necessary for experimental clarification of turbulence models have been published.

In this paper we supply experimental data needed for turbulence models and consider Coriolis force effects on low-Reynolds-number turbulence from similarity laws of turbulence. In § 2 we discuss similarity laws of turbulence as a theoretical background for the present experimental study of turbulence. The experimental setup and method are given in § 3. In § 4 the experimental results and discussion are presented. In § 5 we present conclusions.

2. Similarity laws of turbulence

In our previous publication we studied the similarity laws of the mean velocity distributions for the low-Reynolds-number fully developed two-dimensional turbulent channel flow (Nakabayashi & Kitoh 1996). According to the dimensional analysis, the relevant parameters of this flow are Reynolds number $Re^* = u^* D/\nu$ and the Coriolis parameter $Rc = \Omega\nu/u^{*2}$ for the wall region, and Re^* and $\Omega D/u^*$ for the turbulent core-region. Figure 1(a) shows a schematic of the mean velocity and total shear stress profiles in fully developed two-dimensional rotating channel flow. Here the channel rotates in a counterclockwise direction ($\Omega < 0$), where the $\overline{x}$- and $\overline{y}$-axes are taken to be streamwise and wall-normal on the suction side, respectively. The y-axis is taken to be the wall-normal direction on each side of the wall, figure 1(b). The configurations of the pressure and suction sides in figure 1(a) are reversed when $\Omega > 0$. $2D$, U_c, τ_{ws} and τ_{wp} are the channel width, mean velocity in the central plane of the channel and the wall shear stresses on the suction and pressure sides, respectively. Following the dimensional analysis, the mean velocity normalized by the wall friction velocity u^* can be given by

$$U/u^* = F(yu^*/\nu, \Omega\nu/u^{*2}, u^* D/\nu). \tag{1}$$

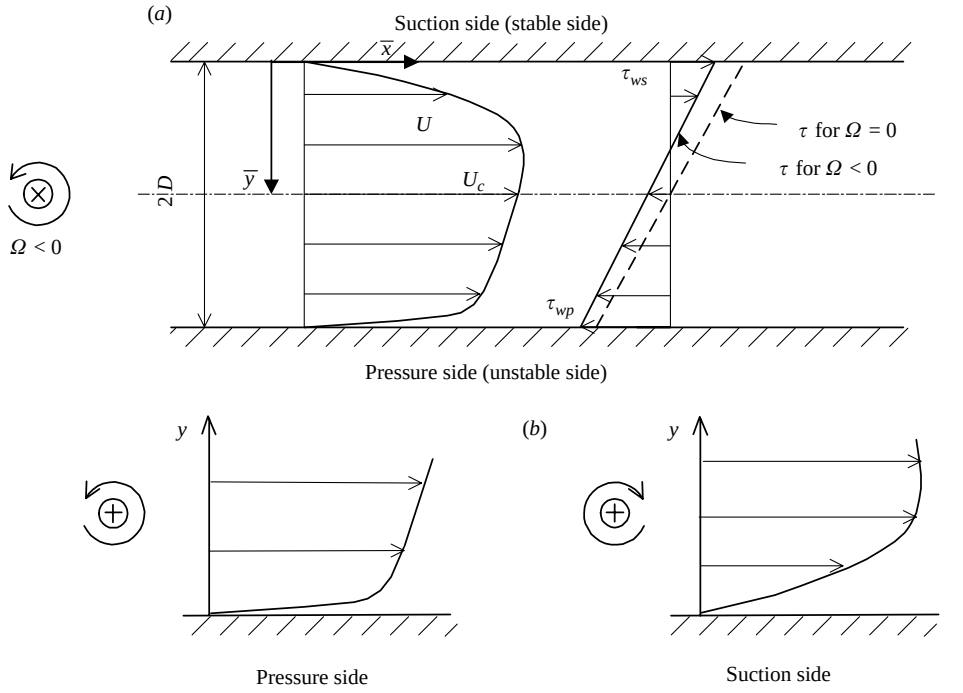

FIGURE 1. Schematic of fully developed two-dimensional flow in a rotating channel. (*a*) Mean velocity and total shear stress profiles. (*b*) Definition of y-axis.

Similar to the mean velocity, the turbulence intensities normalized by the wall friction velocity can be written

$$u/u^*, v/u^*, w/u^* = f(yu^*/\nu, \Omega\nu/u^{*2}, u^*D/\nu) \tag{2a}$$

$$= f(y^+, Rc, Re^*) \tag{2b}$$

$$= f(y/\delta_\nu, \delta_\nu/\delta_c, D/\delta_\nu), \tag{2c}$$

where u, v and w are turbulence intensity in the streamwise, wall-normal and spanwise directions, respectively. Here $\delta_\nu = \nu/u^*$ is the viscous length scale that is a measure of the distance from the wall within which the viscous effect predominates. $\delta_c = u^*/|\Omega|$ is the Coriolis length scale that is a measure of the distance from the wall above which the Coriolis force plays an important role. The channel half-width D is a measure of the outer length scale of the flow. Figure 2 shows the range of each length scale, δ_ν, δ_c and D. These three length scales respectively play a prominent role in the following regions:

$$\text{viscous length scale } \delta_\nu \quad \text{for } y < K_1\delta_\nu, \tag{3a}$$

$$\text{Coriolis length scale } \delta_c \quad \text{for } y > K_2\delta_c, \tag{3b}$$

$$\text{outer length scale } D \quad \text{for } y > K_3 D, \tag{3c}$$

where K_1, K_2 and K_3 are constants.

Very close to the wall, where $y^+ = y/\delta_\nu$ is smaller than K_1, only the viscous length scale is important for the streamwise component u/u^*, because the influence of the Coriolis force does not penetrate close to the wall. So the following expression holds:

$$u/u^* = f_1(y^+). \tag{4}$$

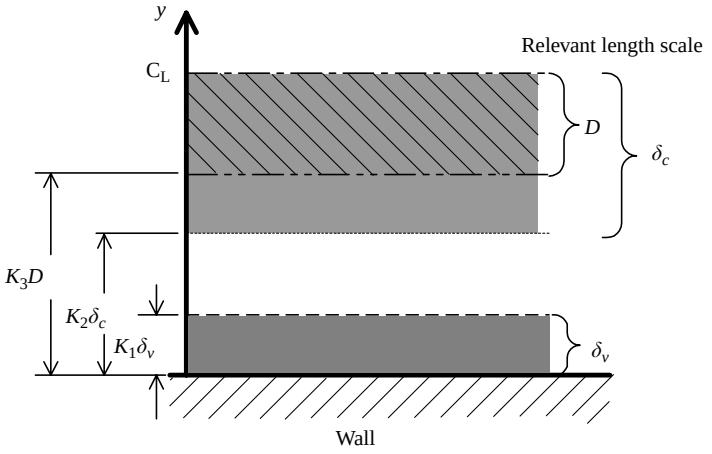

FIGURE 2. Ranges of each length scale involved.

On expanding equation (4), simple momentum and continuity equations applicable immediately adjacent to the wall indicate that

$$u/u^* = A_1 y^+, \tag{5a}$$
$$v/u^* = A_2 y^{+2}, \tag{5b}$$
$$w/u^* = A_3 y^+, \tag{5c}$$

where coefficients A_1, A_2 and A_3 are universal constants when $\Omega = 0$. But when $|\Omega|$ becomes large, $K_2\delta_c$ approaches zero, so that these coefficients become functions of Rc.

In the viscosity-independent region farther from the wall, but not so distant that the Coriolis and outer length scales influence the flow (i.e. $y^+ > K_1$, $y^+ < K_2\delta_c/\delta_v$ and $y^+ < K_3 D/\delta_v$), equation (2) reduces to

$$u/u^* = B_1, \tag{6a}$$
$$v/u^* = B_2, \tag{6b}$$
$$w/u^* = B_3, \tag{6c}$$

where B_1, B_2 and B_3 are constants. We can see plateau regions there.

Moreover, if $|\Omega|$ is increased and the relation $K_3 D > K_2\delta_c$ holds, there exists a Coriolis region for max $(K_1\delta_v, K_2\delta_c) < y < K_3 D$, where only the Coriolis length scale δ_c plays a role in the viscous-independent region farther from the wall. Here, if we introduce a new variable, $y_c^* = y/\delta_c$, the Coriolis region exists in the range

$$\max(K_1|Rc|, K_2) < y_c^* < K_3 R_e^* |Rc|, \tag{7}$$

and the following alternative similarity expression for the turbulence intensity can be obtained:

$$u/u^*, v/u^*, w/u^* = f_2(y_c^*). \tag{8}$$

From a consideration of the Coriolis region in relation to the mean velocity distribution, Nakabayashi & Kitoh (1996) found 30–50, 0.008–0.015 and 0.2–0.3 for K_1, K_2 and K_3, respectively.

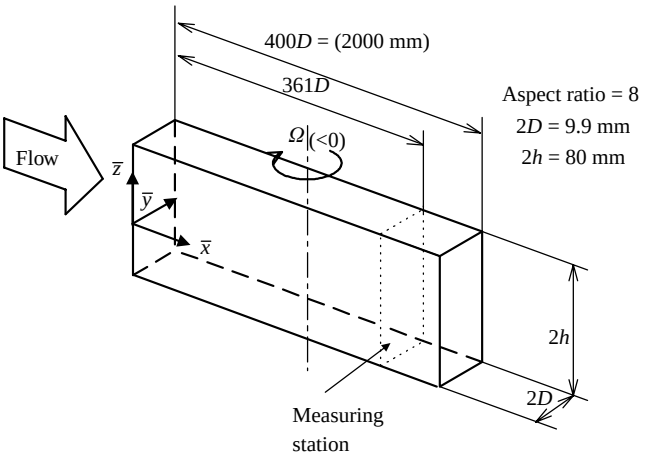

FIGURE 3. Channel geometry and coordinate system.

Run	$Re = 2U_m D/\nu$	$Ro = 2D\lvert\Omega\rvert/U_m$	$R_\Omega = (2D)^2\lvert\Omega\rvert/\nu$	$Re^* = u^* D/\nu$	$Rc = \Omega_v/u^{*2}$	Symbol
1	2500	0	0	83	0	△
2	2500	0.028	70 P	100	0.00171	▲
3	2500	0.056	140 P	107	0.00297	◭
4	2500	0.028	70 S	70	−0.00348	▽
5	2500	0.056	140 S	70	−0.00699	▼
6	3700	0	0	119	0	○
7	3700	0.0189	70 P	141	0.001	●
				141	0.0009	
8	3700	0.0378	140 P	146	0.0016	⊙
				157	0.0014	
9	3700	0.0189	70 S	109	−0.0015	◑
				111	−0.0014	
10	3700	0.0378	140 S	98	−0.0036	◓
				95	−0.0039	
11	5500	0	0	173	0	□
12	5500	0.0127	70 P	183	0.0005	■
13	5500	0.0255	140 P	192	0.0009	▣
14	5500	0.0127	70 S	165	−0.0006	◨
15	5500	0.0255	140 S	158	−0.0014	⬒

TABLE 1. Experimental conditions.

3. Experimental setup and method

The experimental apparatus and method are the same as presented earlier by Nakabayashi & Kitoh (1996). Figure 3 shows the channel geometry and coordinate system. The test channel has a cross-sectional dimension of $2D = 9.9$ mm and $2h = 80$ mm. A measuring station is located at $\bar{x} = 361D$ downstream from the channel inlet section, where the flow is two-dimensional and fully developed for the stationary channel. The values of u' and v' were measured by a single X-probe and a hot-wire anemometer. Tungsten filaments of 3 μm in diameter and 0.5 mm in length are soldered onto the prongs with a separation of 0.1 mm. The measurements were performed under the conditions of bulk Reynolds number $Re = 2U_m D/\nu = 2500$, 3700, 5500 and rotating Reynolds number $R_\Omega = (2D)^2|\Omega|/\nu = 70$, 120, 140, respectively. Table 1 shows

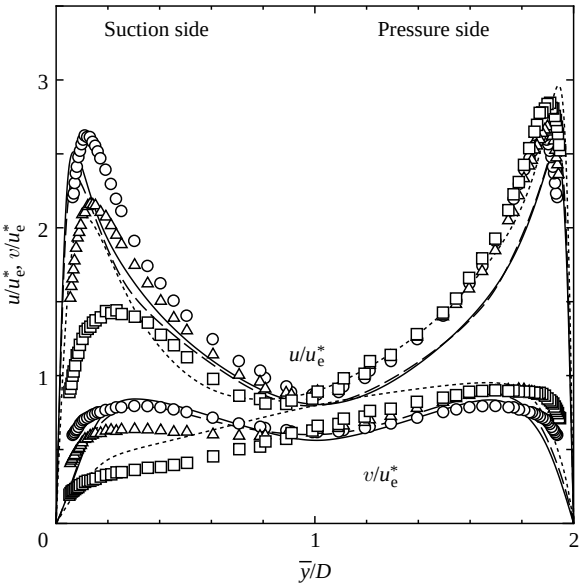

FIGURE 4. Turbulence intensity distribution normalized by u_e^* at $Re = 3700$. Values of R_Ω: ○, 0; △, 70; □, 140. Results of Kristoffersen & Andersson (1993): ———, $Ro = 0$; – – – –, $Ro = 0.01$; · · · · · · · · ·, $Ro = 0.05$.

the experimental conditions for the present measurements. The mean velocity profiles for these parameter combinations were published in our previous paper, Nakabayashi & Kitoh (1996). Positive values of $Rc = \Omega v/u^{*2}$ are found on the pressure side, and negative ones on the suction side. The letters P and S in the column for R_Ω in table 1 indicate the pressure and suction sides of the channel, respectively. Ro is the rotation number $2|\Omega|D/U_m$.

4. Experimental results and consideration

4.1. *Distribution of turbulence intensities*

Figure 4 shows an example of R_Ω dependence of relative turbulence intensities normalized by the effective velocity u/u_e^* and v/u_e^* at $Re = 3700$ in the cross-section of the channel, where u_e^* is an effective velocity defined by

$$u_e^* = \left(\left(u_s^{*2} + u_p^{*2}\right)/2\right)^{1/2}. \tag{9}$$

Here u_s^* and u_p^* are wall friction velocities on the suction and pressure sides, respectively. On the pressure side the increase of u/u_e^* with R_Ω is extremely small, while v/u_e^* shows a slight increase with R_Ω. On the suction side, however, both u/u_e^* and v/u_e^* are significantly decreased by suppression of turbulence. When $R_\Omega = 140$, in particular, turbulence intensities show a large attenuation on the suction side, where relaminarization occurs.

Relative turbulence intensities u/u^* and v/u^* at $Re = 2500$, 3700 and 5500 normalized by the wall friction velocity u_s^* (for $\Omega < 0$) or u_p^* (for $\Omega > 0$) are shown against wall variable y^+ in figures 5(a), 5(b) and 5(c), respectively. The values of u/u^* and v/u^* on the suction side are much smaller than those for the stationary channel flow, and even smaller than those on the pressure side. This is caused by the Coriolis effect. When $Re = 5500$, however, we cannot see a difference among values on the suction

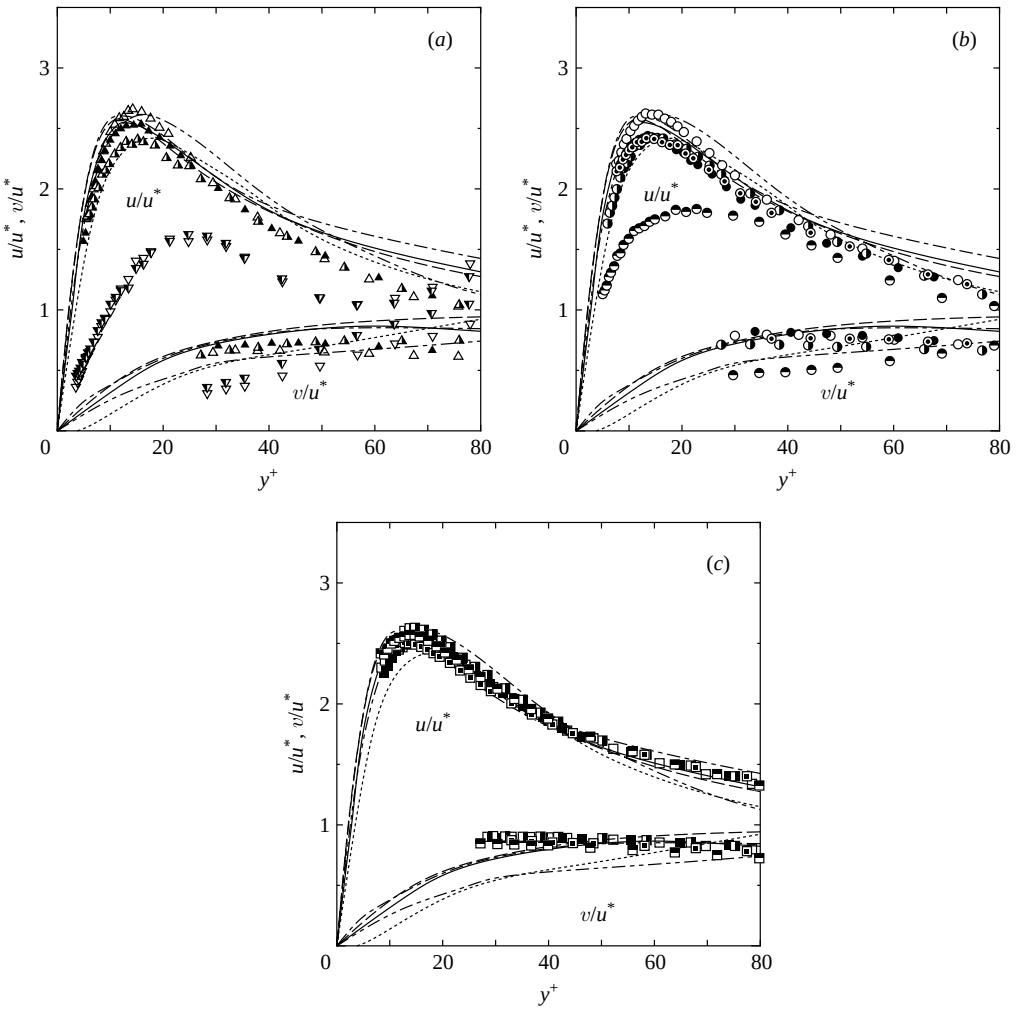

FIGURE 5. Turbulence intensity distribution normalized by u^*. For symbols, see table 1. The values of Rc of Kristoffersen & Andersson (1993) at $Re = 5800$: ———, 0; – – – – –, 0.00161; – – – – –, −0.00322; – – – – –, 0.003; · · · · · · · · ·, −0.00729. (*a*) $Re = 2500$. (*b*) $Re = 3700$. (*c*) $Re = 5500$.

and pressure sides and the stationary flow. As described in Nakabayashi & Kitoh (1996), the Coriolis force effect depends on the Coriolis parameter $Rc = \Omega\nu/u^{*2}$. When the Reynolds number increases, keeping Ω constant, Rc decreases, so that the difference diminishes. DNS results by Kristoffersen & Andersson ($Re = 5800$) are shown in figures 4 and 5, where their u/u^* results show some difference with those for $Re = 2500$, 3700 even though all these cases have a similar Rc value. In particular, the differences are significant when the flows at $Re = 2500$ and 3700 are relaminarized, but the flows of DNS with similar Rc are not. When Re is small, the effect of the outer scale D appears in the near-wall region, and the parameter Re^* enters in the functional form of equation (4). For low Re^*, relaminarization on the suction side depends not only on Rc but also on Re^*.

Very close to the wall, turbulence intensity is governed by equations (5). Figure 6 shows the relation between coefficient A_1 and Coriolis parameter Rc. In the range

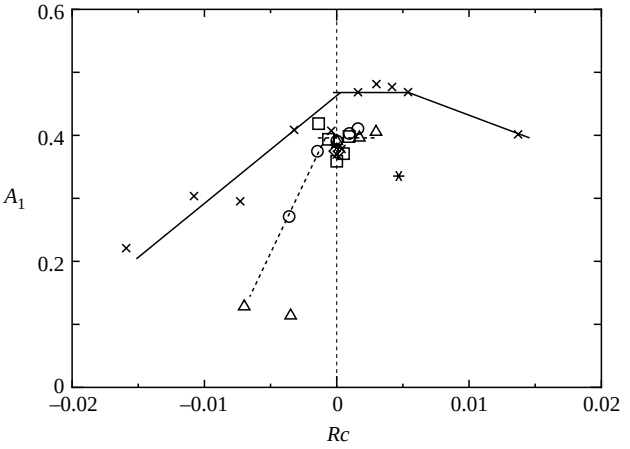

FIGURE 6. Variation of coefficient A_1 with Rc. Re: △, 2500; ○, 3700; □, 5500; ×, 5800 (Kristoffersen & Andersson 1993); ∗, 4710 (Miyake & Kajishima 1998). ◇, Poiseuille flow of Krepelinn & Eckelman (1979), $Re_c = 2DU_c/\nu = 7700$, where U_c is a velocity at channel centre. ———, line joining Kristoffersen & Andersson data; ·····, line joining present data.

$-0.002 < Rc < 0.006$, the present data scatter around a constant value of 0.39 as does the result of Kristoffersen & Andersson (1993) which is a little higher than the present one. When $|\Omega|$ becomes large, A_1 shows a tendency to decrease on the suction side. The present data show a sharper decrease than those of Kristoffersen & Andersson (1993), because relaminarization occurs in the former for a smaller value of $|Rc|$. From skin friction data, relaminarization occurs for $Re = 2500$ when $Rc < -0.0023$ (Nakabayashi & Kitoh 1996). This tendency for A_1 to decrease on the suction side indicates the suppression of turbulence caused by penetration of the Coriolis force effect into the near-wall region.

Here we introduce $y^+_{1\%}$, which is the wall variable at which the u/u^* profile deviates by 1% from the non-rotating profile in figure 5. From the graphs, we can estimate the depth of penetration. If we estimate $y^+_{1\%}$ as the ratio of the distance (which the Coriolis force effect penetrates) to the viscous length scale δ_v, we can take $y = y^+_{1\%}\delta_v = K_2\delta_c$. Then,

$$\log y^+_{1\%} + \log|Rc| = \log K_2. \tag{10}$$

Figure 7 shows the relation between $y^+_{1\%}$ and $|Rc|$, and for comparison the line of $y^+_{1\%}$ obtained from the mean velocity profile (Nakabayashi & Kitoh 1996). Although there is some scatter among the present data, and those of Kristoffersen & Andersson (1993) and Miyake & Kajishima (1988), $y^+_{1\%}$ decreases monotonically along the solid and broken lines indicated by equation (10). Although some Re^*-effect on $y^+_{1\%}$ in low-Reynolds-number flow ($Re = 2500$, 3700) might be expected, figure 7 suggests a definite $|Rc|$ dependence of $y^+_{1\%}$. The broken line is for $K_2 = 0.005$ and the solid line for $K_2 = 0.015$. $K_2 = 0.008$–0.015 was obtained from the data of the mean velocity profile (Nakabayashi & Kitoh 1996).

Figure 8 shows the Coriolis region in the $(y^*_c, |Rc|)$-plane. In the figure, a broken line and a chain double dot line indicate the relations $y = K_1\delta_v$ and $y = K_2\delta_c$, respectively. The upper area of these lines (grey shaded area) satisfies the left-hand side of inequality (7). Solid lines indicate the relation $y = K_3 D$ for different Re^*. The lower area of each line, denoted by hatching, satisfies the right-hand side of inequality (7). For the Coriolis region, the Reynolds number has to satisfy $Re^* > K_1/K_3$. From this

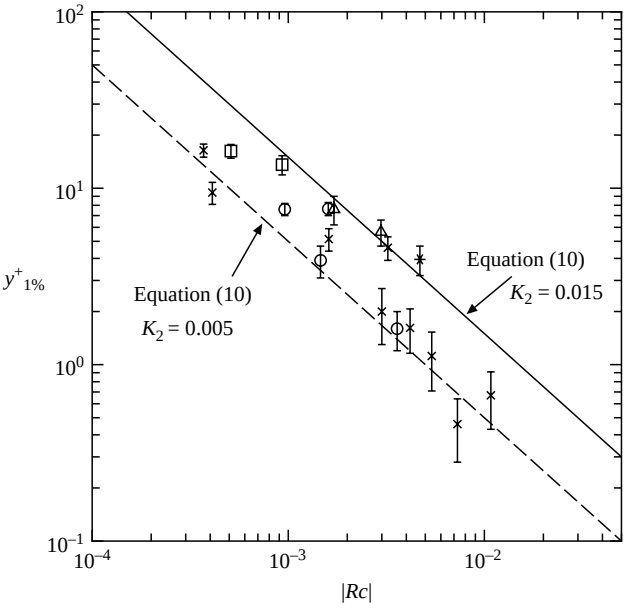

FIGURE 7. Coriolis penetration depth $y_{1\%}$ as a function of Coriolis parameter Rc. Re: △, 2500; ○, 3700; □, 5500; ×, 5800 (Kristoffersen & Andersson 1993); *, 4710 (Miyake & Kajishima 1988).

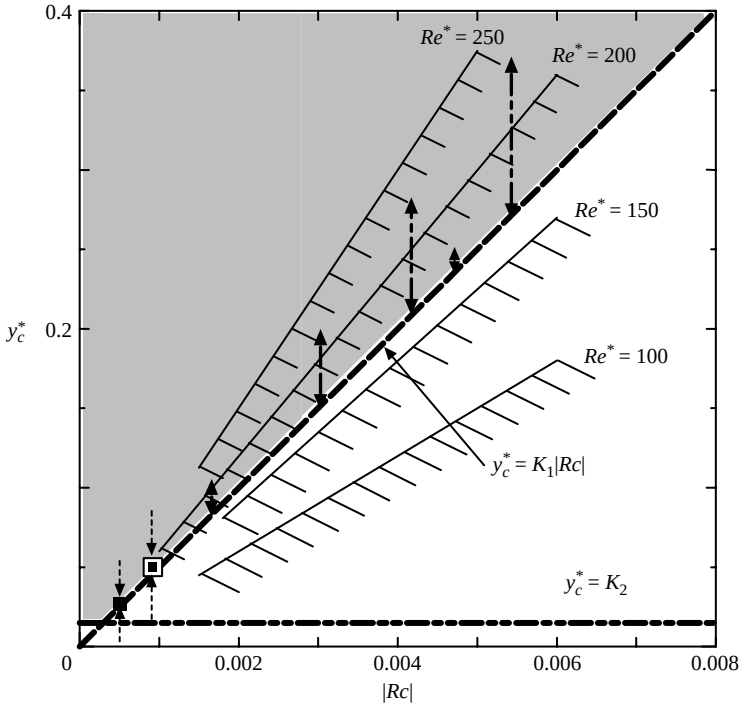

FIGURE 8. Coriolis region for various conditions. Shading and hatching indicate the boundaries of each inequality relation for the Coriolis region. Double-arrow lines indicate range of the Coriolis region. For symbols, see table 1. Values of Re^* for DNS results by Kristoffersen & Andersson (1993): – – – –, 210; · · · · · · · · ·, 220; – – – – – –, 230; – – – – – – – – – – –, 230; and LES results by Miyake & Kajishima (1988): ———, 180.

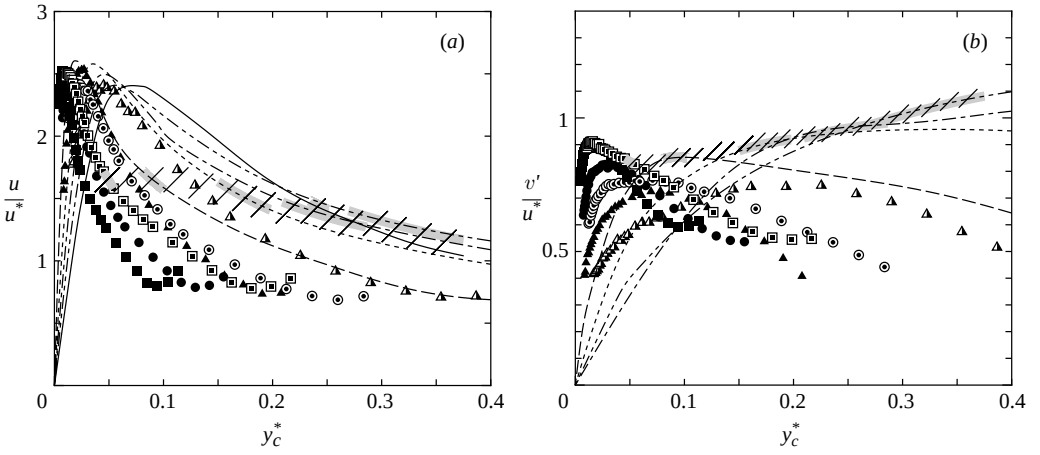

FIGURE 9. Universal turbulence intensity distribution in the Coriolis region. For symbols, see table 1. The shaded area is the Coriolis region for each condition estimated by assuming $K_1 = 50$, $K_2 = 0.0015$ and $K_3 = 0.3$. The hatched area indicates the estimated universal turbulence intensity profile for the Coriolis region drawn as an overall curve of shaded regions. The values of Rc for Kristoffersen & Andersson (1993) for $Re = 5800$: – – –, 0.00161; · · · · · · · · · · · ·, 0.003; – – – – – – – –, 0.00418; – – – – – – – –, 0.00539; and for Miyake & Kajishima (1988) for $Re = 4710$: ——— 0.00469. (*a*) Streamwise velocity component. (*b*) Wall-normal velocity component.

figure, it is evident that high $|Rc|$ as well as high Re^* are necessary for the Coriolis region. The range covered by each arrow is the estimated Coriolis region for various conditions, including the DNS by Kristoffersen & Andersson as well as the present experiment. The present results for $Re = 5500$ are marginally in the Coriolis region because of low $|Rc|$.

Figures 9(*a*) and 9(*b*) shows the turbulence intensity against y_c^*. The Coriolis region whose range is calculated from inequality (7) with $K_1 = 50$, $K_2 = 0.015$ and $K_3 = 0.3$ is indicated by the shaded area for each condition. The overall curve of the shaded areas, indicated by hatching, constitutes a similarity distribution, equation (8) in the Coriolis region, though the overall curve for u/u^* is not very smooth, perhaps due to the unrefined values of K_1, K_2 and K_3. The hatched area shows that u/u^* decreases almost linearly from 1.7 to 1.2 with an increase of y_c^* from 0.05 to 0.4 in the Coriolis region. On the other hand, v/u^* increases from 0.8 at $y_c^* = 0.05$ to 1.1 at $y_c^* = 0.4$.

Figures 10(*a*) and 10(*b*) show the R_Ω dependence on shear stress distributions measured at $Re = 2500$ and 3700 by an X-probe in the cross-section of the channel. Reynolds shear stress is augmented on the pressure side and reduced on the suction side. The Reynolds shear stress profile for $Re = 2500$ at $R_\Omega = 140$ shows that perfect relaminarization occurs on the suction side as the Reynolds shear stress becomes zero.

In the present experiment, the measuring station is located at an inlet length ($\overline{x}/D = 361$), sufficient to ensure fully developed flow and the measured shear stress follows a linear distribution, as can be seen at $R_\Omega = 0$. For the rotating channel, however, the shear stress profiles are curved on the pressure side in contrast to the straight ones expected for fully developed two-dimensional flow. The main reason for the curved profiles is the existence of roll cells developed on the pressure side. The shear stress is affected by the inertia term I through roll cell velocity components V and W (V and W are wall-normal and spanwise mean velocity components)

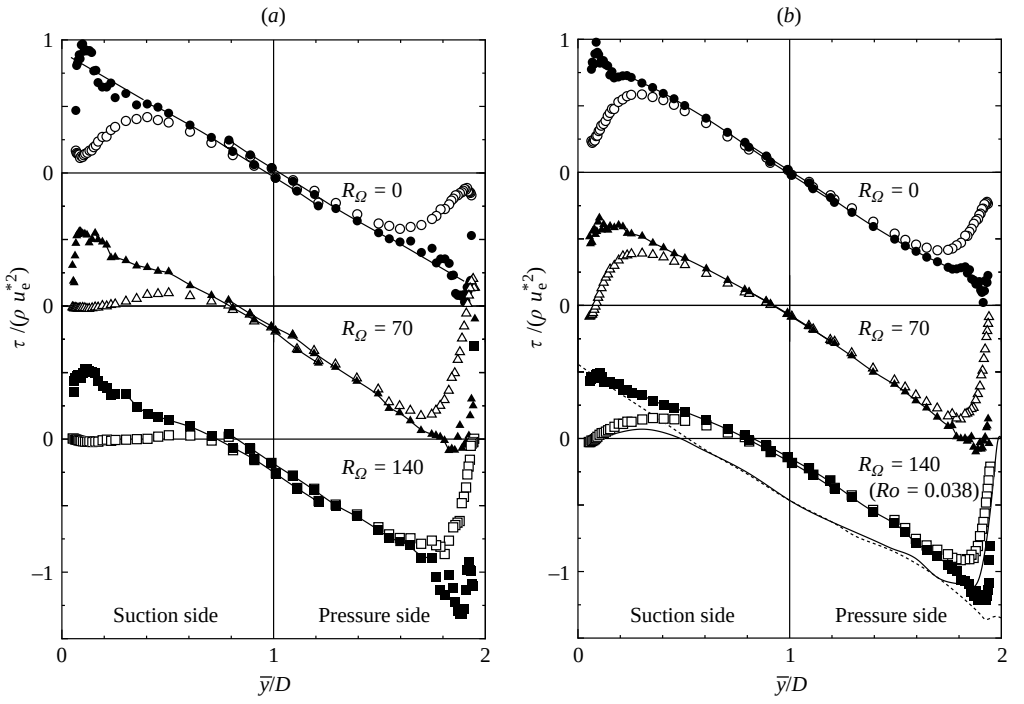

FIGURE 10. Total shear stress and Reynolds shear stress distribution. (*a*) $Re = 2500$, (*b*) $Re = 3700$: ●, ▲ and ■, Total shear stress. ○, △ and □, Reynolds shear stress. Miyake & Kajishima (1988) for $Re = 4710$ and $Ro = 0.12$: – – – –, total shear stress; ———, Reynolds shear stress.

as follows:

$$\tau = \tau_w + (\mathrm{d}p/\mathrm{d}x)y + \int_0^y I\,\mathrm{d}y, \tag{11}$$

where I denotes the inertia term and is given by

$$I = \rho(V\partial U/\partial y + W\partial U/\partial z - 2\Omega V). \tag{12}$$

In accordance with the experimental results for the rotating channel by Johnston *et al.* (1972) and the curved channel by Barlow & Johnston (1988), roll cells of Taylor–Görtler type occur randomly in space as well as in time, and do not remain at a preferred location. Consequently, mean values of V and W become zero, so that the inertia term given by equation (11) becomes zero. However, as Watmuff *et al.* (1985) reported, the inevitable inlet disturbance at the inlet section of the duct, even in a two-dimensional flow configuration without the endwall effect, causes quasi-stationary roll cells on the pressure side, and non-zero velocity components V and W may appear. Kristoffersen & Andersson (1993) also reported the quasi-stationary roll cells in their DNS and discussed the various reasons for them to appear in numerical simulation.

4.2. *Effect of Coriolis force on Reynolds stress transport*

The effect of the Coriolis force on the distribution of each Reynolds normal and shear stress component indicated in §4.1 was examined by investigating the size of each term that appears in Reynolds stress transport equations. The Reynolds stress

transport equations under discussion here expressed using wall variables are

$$\frac{\mathrm{D}}{\mathrm{D}t^+}\left(\frac{u^2}{u^{*2}}\right) = \underbrace{-2\frac{\overline{u'v'}}{u^{*2}}\frac{\mathrm{d}U^+}{\mathrm{d}y^+}}_{\text{production term}} + \underbrace{4\frac{\overline{u'v'}}{u^{*2}}\frac{\Omega\nu}{u^{*2}}}_{\text{Coriolis term}} + \Phi^+_{u^2} + D^+_{u^2} - \epsilon^+_{u^2}, \tag{13}$$

$$\frac{\mathrm{D}}{\mathrm{D}t^+}\left(\frac{v^2}{u^{*2}}\right) = \underbrace{-4\frac{\overline{u'v'}}{u^{*2}}\frac{\Omega\nu}{u^{*2}}}_{\text{Coriolis term}} + \Phi^+_{v^2} + D^+_{v^2} - \epsilon^+_{v^2}, \tag{14}$$

$$\frac{\mathrm{D}}{\mathrm{D}t^+}\left(-\frac{\overline{u'v'}}{u^{*2}}\right) = \underbrace{\frac{v^2}{u^{*2}}\frac{\mathrm{d}U^+}{\mathrm{d}y^+}}_{\text{production term}} + \underbrace{2\frac{\Omega\nu}{u^{*2}}\frac{u^2-v^2}{u^{*2}}}_{\text{Coriolis term}} + \Phi^+_{-uv} + D^+_{-uv} - \epsilon^+_{uv}, \tag{15}$$

where $t^+ = t/(\nu/u^{*2})$, Φ^+ is the pressure–strain correlation term, D^+ is the diffusion term, and ϵ^+ is the turbulent energy dissipation term. On the right-hand side of the above equations, the terms including $\Omega\nu/u^{*2}(=Rc)$ are the Coriolis terms. As has been elucidated in research to date, from equations (13) and (14), the turbulent energy is produced for u^2, and part of this is transported to v^2 or w^2 by the Coriolis and pressure–strain correlation terms. The Coriolis term transports energy from u^2 to v^2 on the pressure side ($\Omega > 0$), and from v^2 to u^2 on the suction side ($\Omega < 0$). In this way the qualitative characteristics of the Coriolis terms can be understood. Andersson & Kristoffersen (1995) and Kristoffersen *et al.* (1990) reported the detailed budget of the terms in the transport equations using their DNS data and showed the characteristic features of the stress transport in rotating channel flow. Here we confirm their results from the experimental point of view.

Of all terms in equations (13)–(15), the only ones estimated from the observed $U^+(y^+)$ and the turbulence data are the production and Coriolis terms. Using these terms, the extent of the relative contribution of the Coriolis term can be understood, as shown in figures 11 and 12.

Concerning u^2/u^{*2} (figure 11), the amount transported by the Coriolis term, even with large changes in the velocity distribution (from $R_\Omega = 140$ P to 140 S), is extremely small compared to the production term and makes virtually no contribution to turbulent energy transport. The production term is decreased on the pressure side by the effect of the rotation, and this is considered to be the cause of the decline of u/u^* on the pressure side as indicated in figure 5. The decline in the production term on the pressure side is caused by a large decline in the mean velocity gradient $\mathrm{d}U^+/\mathrm{d}y^+$ on the pressure side, as shown in figure 13. On the other hand, because $\mathrm{d}U^+/\mathrm{d}y^+$ is very large on the suction side, the production term is about the same size as in a stationary channel even with a decline in Reynolds shear stress $-\overline{u'v'}/u^{*2}$ on the suction side.

Next, we consider the transport of Reynolds shear stress $-\overline{u'v'}/u^{*2}$ for each transport term, shown in figure 12. The production term on the pressure side is small compared to that for stationary channel flow or on the suction side because, as can be seen in figure 13, the mean velocity gradient $\mathrm{d}U^+/\mathrm{d}y^+$ is small on the pressure side. It is known that the Coriolis term acts as a $-\overline{u'v'}$ producer on the pressure side and as a suppressor on the suction side. Its size is about $1/3$ that of the production term on the pressure side and $1/2$ that on the suction side. This means that the Coriolis term makes a large contribution to the Reynolds shear stress transport.

As pointed out above, the Coriolis effect causes changes in the Reynolds shear stress by working directly upon shear stress $-\overline{u'v'}/u^{*2}$, and the velocity distribution

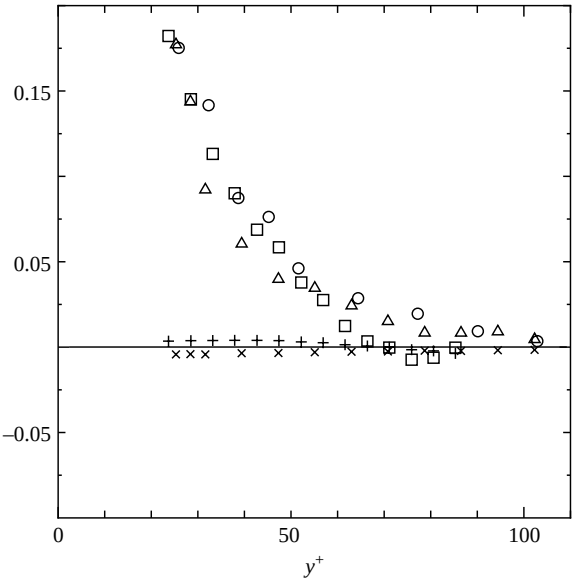

FIGURE 11. Contribution of Coriolis term to u^2/u^{*2} transport. $Re = 3700$. Open symbols, production term; + and ×, Coriolis term. The values of Rc: ○, 0; △ and ×, 0.0014; □ and +, −0.0039.

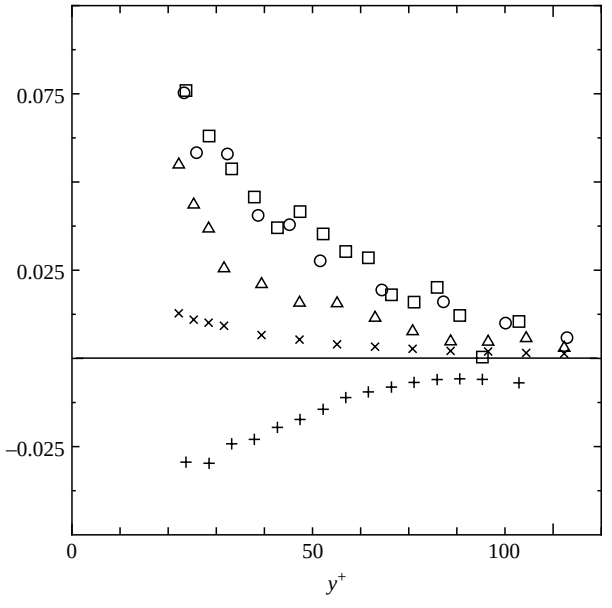

FIGURE 12. Contribution of Coriolis term to $\overline{u'v'}/u^{*2}$ transport. For legend, see figure 11.

$U^+(y^+)$ is changed as a result. However, the direct effect of the Coriolis force on the Reynolds normal stress u^2/u^{*2} is extremely small, and it exerts an indirect effect through the changes in the velocity gradient $\mathrm{d}U^+/\mathrm{d}y^+$, $-\overline{u'v'}/u^{*2}$ and perhaps also the pressure–strain term.

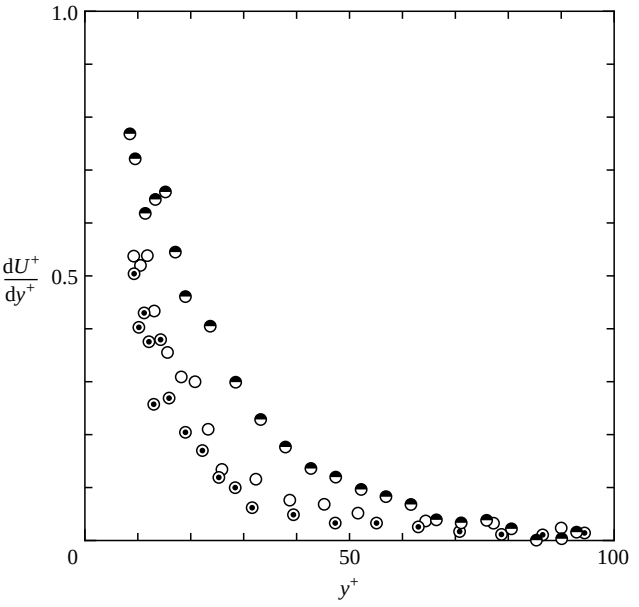

FIGURE 13. Velocity gradient expressed in wall variables for stationary channel and pressure and suction sides of channel. For symbols, see table 1.

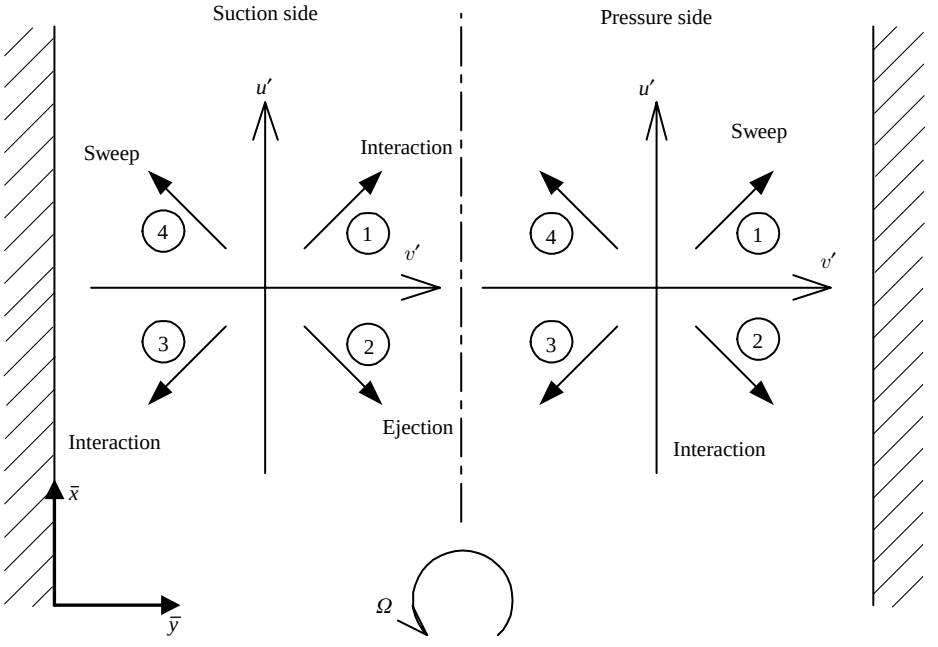

FIGURE 14. Coordinate and quadrants on pressure and suction sides, respectively.

The above picture of the Reynolds stress transport u^2/u^{*2} and $-\overline{u'v'}/u^{*2}$ is consistent with that of Andersson & Kristoffersen (1995). According to them the budget of v^2/u^{*2}, not given here, is rather complicated compared to u^2/u^{*2}, because no dominant transport exists. The relative importance of the Coriolis term on the transport of v^2/u^{*2} was shown to be large.

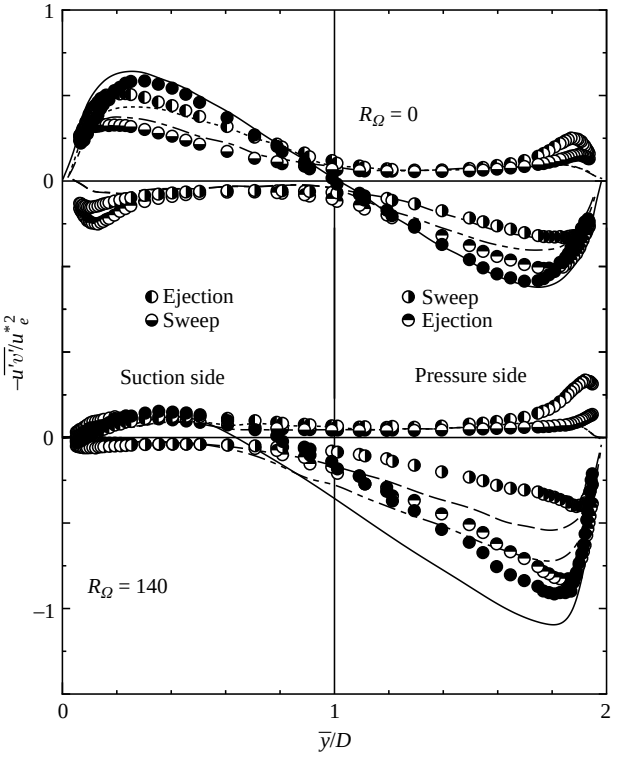

FIGURE 15. Contribution from each quadrant to Reynolds shear stress for $Re = 3700$. Quadrant: ◑, 1st; ◐, 2nd; ◓, 3rd; ◒, 4th; ●, Total. Quadrant from Miyake & Kajishima (1986) for $R_\Omega = 0$ and $R_\Omega = 500$ having $Re^* = 250$: – – – –, 1st; · · · · · · · · ·, 2nd; – – – – – – – – –, 3rd; – – – – – –, 4th; ———, total.

4.3. *Four-quadrant analysis, correlation coefficient, and higher statistics*

In § 4.2 we found that the rotation effect works directly on the Reynolds shear stress through the Coriolis term. Here we examine that effect in more detail. Frequency and fractional contributions to the Reynolds shear stress from each velocity quadrant are studied by four-quadrant analysis. The coordinate system and quadrants used here are shown in figure 14. Figure 15 shows the four-quadrant analysis of $-\overline{u'v'}/u_e^{*2}$ for stationary channel flow ($R_\Omega = 0$) and rotating channel flow ($R_\Omega = 140$ P and S), figure 16 shows the respective frequency with which they appear in each quadrant. Miyake & Kajishima (1986) pursued a similar discussion using the results of LES. According to those investigations, the increase in Reynolds shear stress on the pressure side comes mainly from the increase in ejection. The contribution of sweep and interaction is of the same magnitude as in a stationary channel. Kristoffersen & Andersson (1993) also reported that the relative contribution of ejection increases on the pressure side. For the frequency distribution of each quadrant, the sweep is large compared to a stationary channel, interaction is low, and ejection is at the same level. On the suction side, the contributions of both ejection and sweep to $-\overline{u'v'}$ are lowered, and the Reynolds shear stress is reduced. As for frequency distribution, the sweep declines and interaction in quadrant 1 partly increases. In this connection, an anomalous increase in the relative contribution from quadrant 1 interaction was reported by Kristoffersen & Andersson (1993). On the pressure side, the contribution of ejection to $-\overline{u'v'}$ is large even though the frequency is not high. Miyake & Kajishima

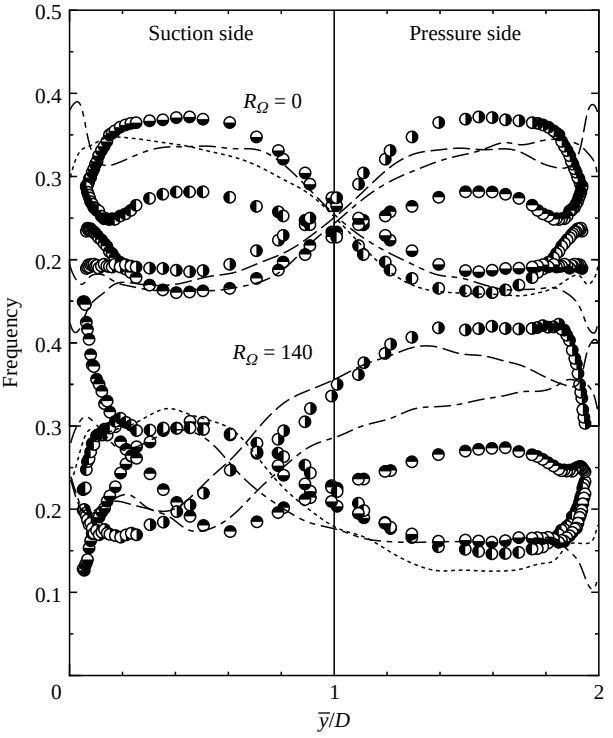

FIGURE 16. Frequency of each quadrant for $Re = 3700$. For legend, see figure 15.

(1986) have stated that this phenomenon is due to the effect of the Coriolis force thrusting high-speed fluid against the wall on the pressure side, and the accompanying forcing out of low-speed fluid from the wall.

This phenomenon is investigated here by simultaneous recordings of fluctuations u' and v'. Figure 17 compares the time series of fluctuations u', v', and $u'v'$ at $y^+ = 45$ with those for the stationary channel and $R_\Omega = 140$ P. The ejection process ($u' < 0$, $v' < 0$, $u'v' > 0$) occurs randomly in the stationary channel, but develops very strongly on the pressure side of the rotating channel at the times indicated by the vertical dashed lines in figure 17. This occurrence is somewhat cyclical. Since this kind of strong ejection occurs, the contribution to $-\overline{u'v'}$ must be large despite a low ejection frequency on the pressure side. The relation between the non-dimensional value $\Delta T U_m/D$ of the average cycle ΔT for this strong ejection and the non-dimensional cycle $U_m/(\Omega D)$ of the channel rotation is shown in figure 18. The determination of ΔT is somewhat subjective, but from figure 18 a large-scale structural turbulence having a time scale of $1/\Omega$ is assumed to exist on the pressure side of the rotating channel. This structural turbulence gives rise to strong ejection, and the Reynolds shear stress on the pressure side increases. This large-scale turbulence would seem to correspond to the large vortex concentration in the LES results of Miyake & Kajishima (1986) (cf. figure 6 in their paper). This kind of turbulence is also seen in the spectrum analysis described later. It is a special characteristic of rotating channel turbulence, so it is not produced in ordinary wall turbulence.

Figure 19 shows the distribution of the turbulence correlation coefficient $-\overline{u'v'}/(uv)$. The results for stationary channels, except near the wall, agree closely with the DNS results of Kim, Moin & Moser (1987). For the case of rotating channels, however,

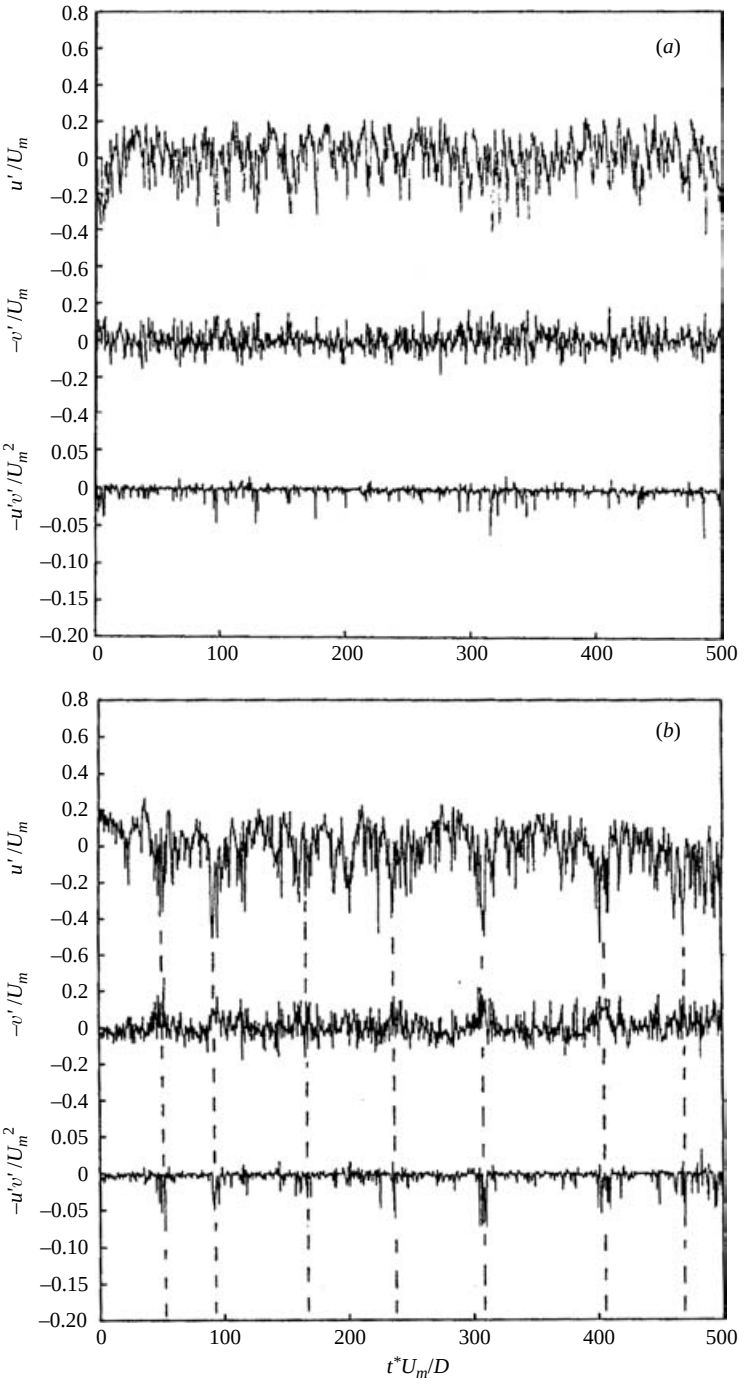

FIGURE 17. Time series of u', v' and $u'v'$ showing strong ejection appearing quasi-periodically at $y^+ = 45$ for $Re = 3700$. R_Ω: (*a*) 0; (*b*) 140 P.

the value of the correlation coefficient increases on the pressure side and decreases on the suction side. This trend is consistent with the analogous results reported by Kristoffersen & Andersson (1995). In figure 19, this is compared with the results

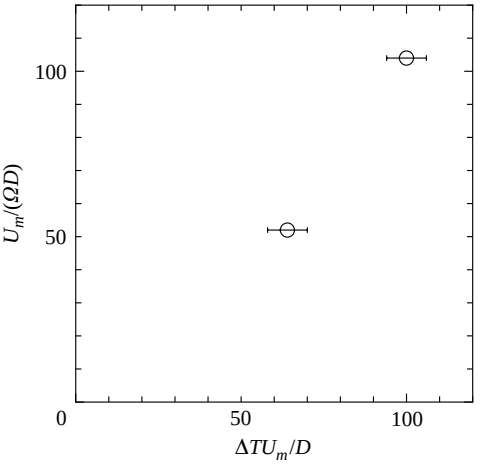

FIGURE 18. Period of strong ejection versus rotation-related parameter.

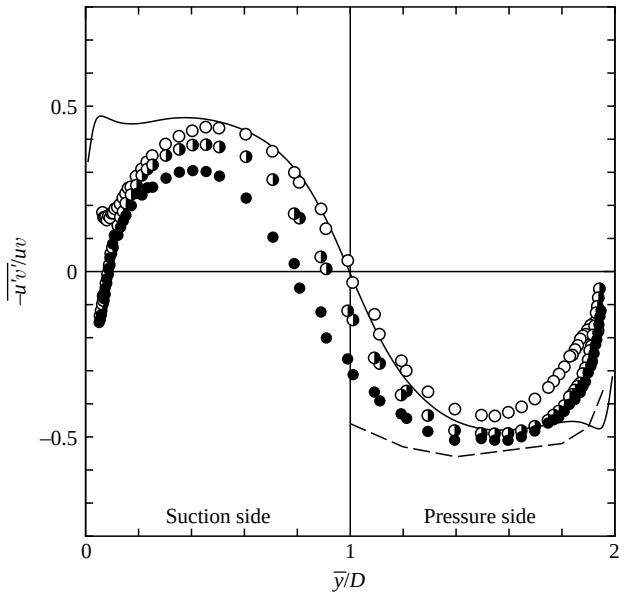

FIGURE 19. Correlation coefficient distribution for $Re = 3700$. $|R_\Omega|$: ○, 0; ◑, 70; ●, 140. ———, DNS of Poiseuille flow by Kim *et al.* (1987) for $Re = 5600$; – – – –, Barlow & Johnston (1988) for curved boundary layer.

of Barlow & Johnston (1988) for curved boundary layer flow on concave surfaces. The results tend to be the same as for the pressure side. Because the correlation coefficient has almost no dependence on the Reynolds number (see Kim *et al.* 1987), it is conjectured that the distribution shown in figure 19 is the same for high Reynolds numbers.

Figure 20 shows the u' and v' skewness factors. The skewness factor $S(v')$ deviates to the negative side as the rotation effect becomes stronger. In contrast, the skewness factor $S(u')$ deviates in the positive direction on the suction side and in the negative direction on the pressure side. For a stationary channel, because the ejection appears in a burst process at $y^+ \geqslant 10$, the u' skewness takes a negative value. On the suction

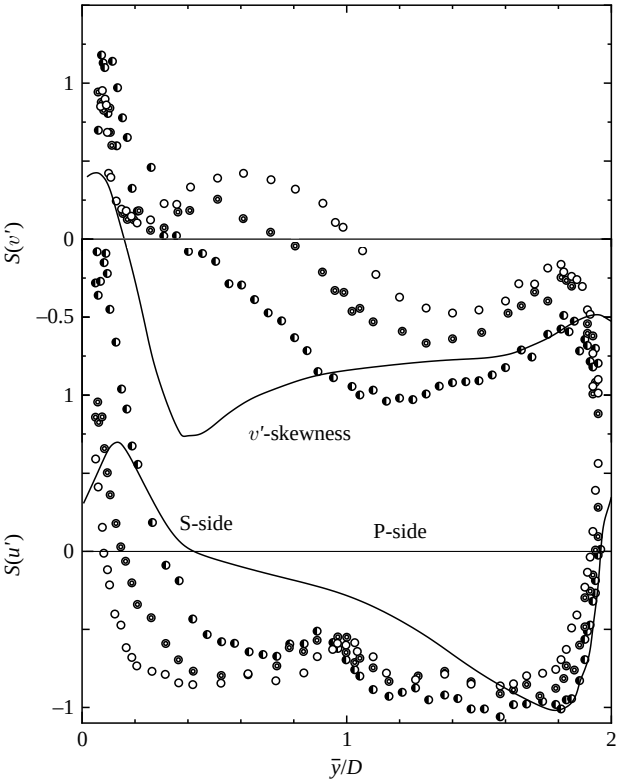

FIGURE 20. Skewness factors for u' and v'. $Re = 3700$. $|R_\Omega|$: ○, 0; ◎, 70; ◐, 140; ———, 565 (Miyake & Kajishima 1988).

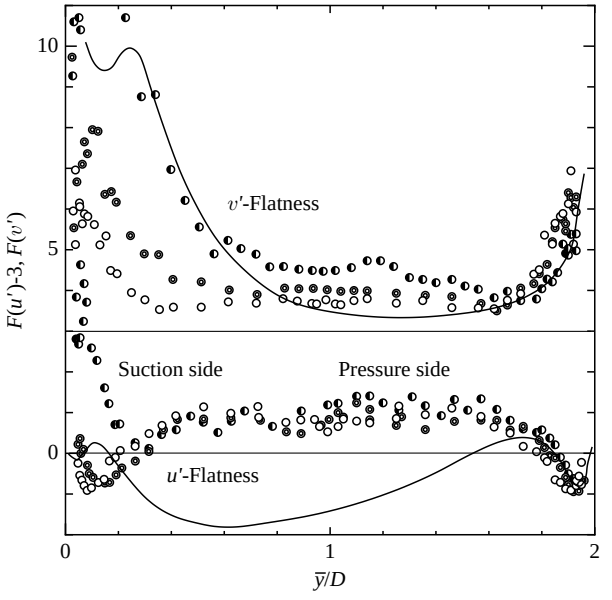

FIGURE 21. Flatness factors for u' and v'. For legend, see figure 20.

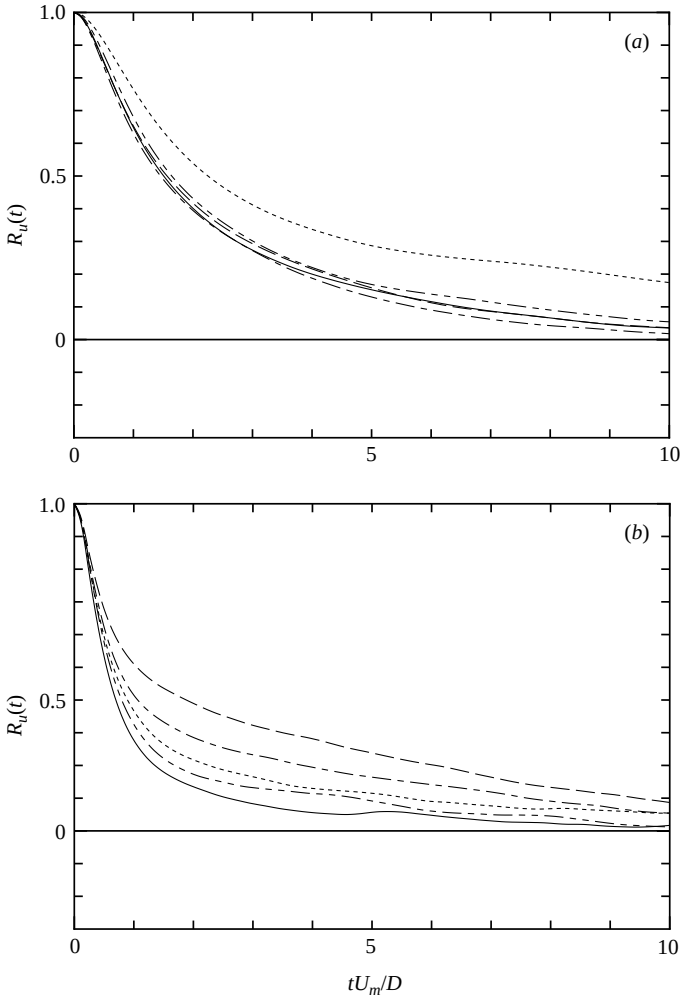

FIGURE 22. Autocorrelation coefficient of $u'(t)$ for $Re = 3700$. (*a*) At $y^+ = 15$. (*b*) At $y^+ = 80$. R_Ω: ———, 0; – – – – –, 70 P; – – – – – – – – –, 70 S; – – – –, 140 P; · · · · · · · · · · · ·, 140 S.

side of a rotating channel, the decreased frequency of bursts causes the u' skewness to deviate to the positive side, because the Coriolis force acts to suppress turbulence. On the pressure side the opposite is true (i.e. increased burst activity causes deviation to the negative side). The results of Miyake & Kajishima (1986) in the same figure show the same qualitative trends, but the influence of the Coriolis force on their flow is larger than in the present experiment, so the above tendencies are more marked.

Figure 21 shows the distribution of the u' and v' flatness factors $F(u') - 3$ and $F(v')$. Near the wall on the pressure side, there is no change in either $F(u') - 3$ or $F(v')$ from the case of a stationary channel, but at $\overline{y}/D \leqslant 1.6$ an effect of rotation appears. For v', with $\overline{y}/D \leqslant 0.6$, the flatness suddenly becomes larger as R_Ω increases. The change in u' flatness from that of a stationary channel is comparatively small; however, for the large R_Ω of Miyake & Kajishima, the flatness becomes smaller and a large difference in qualitative trend is evident.

Figures 22(*a*) and 22(*b*) show the definite difference in the autocorrelation coefficient $R_u(t)$ between $y^+ = 15$ and 80 in the streamwise velocity fluctuation at $Re = 3700$. Except for the relaminarized flow with $R_\Omega = 140$ S, there is no difference in the

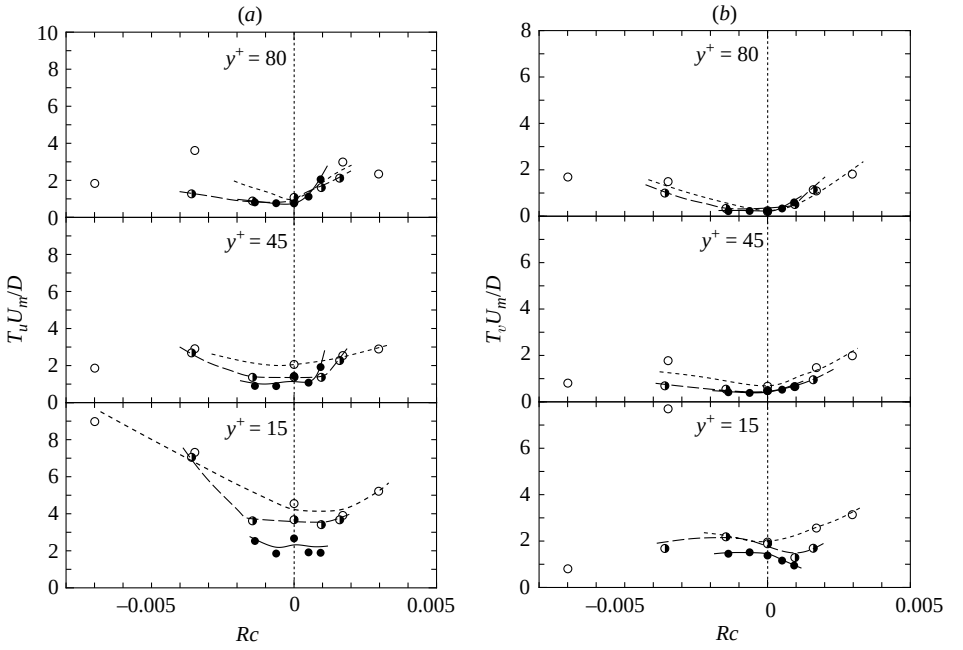

FIGURE 23. Variation of integral scale of u' and v' with Coriolis parameter at various positions. (*a*) T_u, (*b*) T_v. *Re*: ○, 2500; ◑, 3700; ●, 5500.

distribution of $R_u(t)$ at $y^+ = 15$ among the pressure side, the suction side and the stationary channel flow. At $y^+ = 80$, however, there is a definite difference among them. On the pressure side, the distribution curve decreases more slowly than the curves for the suction side and the stationary channel. This means that a larger structure like a roll cell exists on the pressure side but not on the suction side.

Figure 23 shows integral time scales T_u and T_v of $R_u(t)$ and $R_v(t)$, respectively scaled by the outer time scale D/U_m. With decreasing *Re*, the scaled integral time scale of the u' component increases near the wall at $y^+ = 15$ for $Rc < 0$ because of relaminarization. On the other hand, the influences of *Re* and *Rc* are smaller at $y^+ = 45$ and 80 than at $y^+ = 15$. The effect of rotation becomes clear far from the wall on the pressure side, and the integral scale increases with *Rc*.

We can conjecture from this result that a large-scale longitudinal structure exists for $y^+ > 15$, as described before. But there is no clear influence of *Re* on the integral scale of $R_v(t)$.

4.4. *Energy spectrum*

The power spectrum $E_u(k)$ of the velocity fluctuation components u' can be normalized and expressed as follows:

$$1 = \int_0^\infty k^* \tilde{E}_u(k^*)\, \mathrm{d}(\ln k^*), \tag{16}$$

where

$$\tilde{E}_u(k^*) = E_u(k)/(Du^2), \quad k^* = Dk. \tag{17}$$

Here k is the wavenumber and is given by $k = 2\pi f/U$ from the assumption of frozen turbulence. The frequency of the time series signal is f, and the local mean velocity is U. Figure 24 shows the experimental value $k^* \tilde{E}_u(k^*)$ at $y^+ = 80$. The minute element of area $k^* \tilde{E}_u(k^*)\, \mathrm{d}(\ln k^*)$ on the logarithmic axis of k^* in this figure is the power of u' corresponding to $k^+ \tilde{E}_u(k^+)$. For the stationary channel and on the suction side

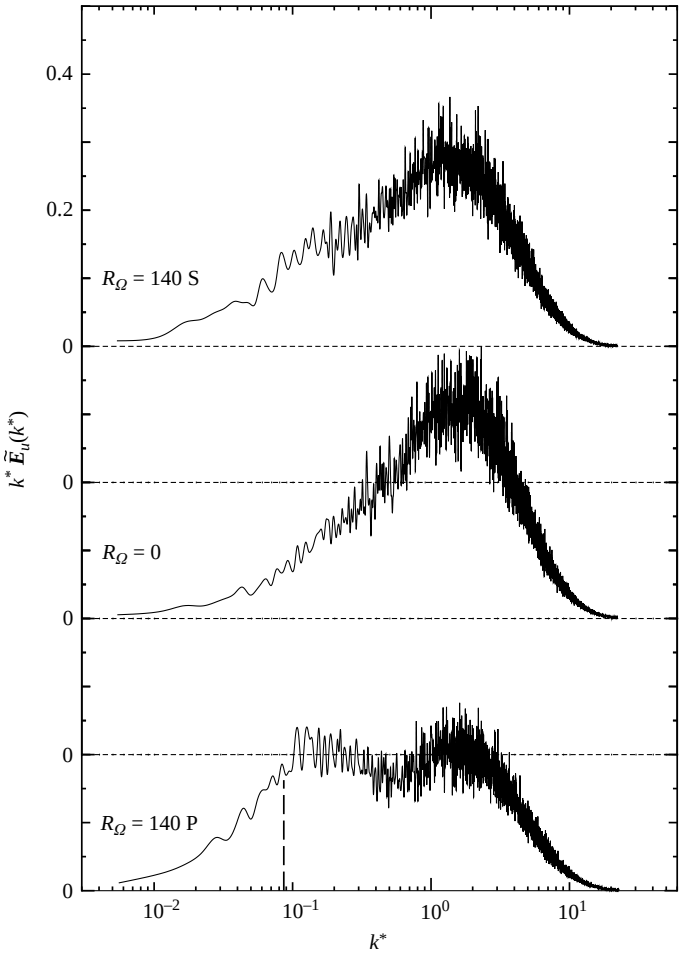

FIGURE 24. Pre-multiplied power spectra of u'. $Re = 3700$ at $y^+ = 80$.

of the rotating channel, both have similar distribution shapes, but on the pressure side a rise in the spectrum is seen in the low-frequency range. The dashed line in figure 24 indicates the frequency corresponding to the cyclic variation of u' mentioned in § 4.3. This rise in the low-frequency range of the spectrum seems to be connected to the gentle cyclic movements caused by the Coriolis force.

5. Conclusion

The present measurements of turbulence in a rotating channel flow indicate the following results.

(i) Relative turbulence intensities near the wall normalized by wall variable are lower than those of stationary channel flow both on the pressure and suction sides. In the near-wall region, the wall variable $y^+_{1\%}$ at which the u/u^* profile deviates by 1% from the non-rotating profile is independent of Reynolds number Re^*, but depends only on the Coriolis parameter Rc. The Coriolis force effect penetrates the viscous wall layer further with increasing Rc.

(ii) The Coriolis region where u/u^* and v/u^* have respective universal functions of y^*_c was confirmed on the pressure side.

(iii) The amount of Reynolds normal stress u^2/u^{*2} transported by the Coriolis term is extremely small compared to the production term in the transport equation. However, the Coriolis term makes a large contribution to Reynolds shear stress transport on the pressure side as well as on the suction side of the channel.

(iv) The increase in Reynolds shear stress on the pressure side is caused by strong ejection, which occurs quasi-periodically on the pressure side due to the Coriolis effect even though the ejection frequency is low.

(v) From the results for the autocorrelation coefficient and integral time scale, we conjecture that a large-scale longitudinal structure like the roll cell exists on the pressure side and that it influences ejection at a position far from the wall. On the pressure side, a rise in the spectrum which is relevant to a bursting phenomenon excited by the roll cell's motion is seen in the low-frequency range that corresponds to the observed strong ejection.

The authors would like to express their appreciation to Mr Y. Konishi and Mr M. Aoki for their assistance in performing the experimental works and the data processing. This work was financially supported through a Grant-in-Aid (No. 02650132) by the Ministry of Education, Culture, Sports, Science and Technology, Japan.

REFERENCES

Andersson, H. I. & Kristoffersen, R. 1995 Turbulence statistics of rotating channel flow. In *Turbulent Shear Flows 9, Selected Papers* (ed. F. Durst *et al.*), pp. 53–70. Springer.

Barlow, R. S. & Johnston, J. P. 1988 Structure of a turbulent boundary layer on a concave surface. *J. Fluid Mech.* **191**, 137–176.

Bradshaw, P. 1969 The analogy between streamline curvature and buoyancy in turbulent shear flow. *J. Fluid Mech.* **36**, 177–191.

Johnston, J. P., Haleen, R. M. & Lezius, D. K. 1972 Effects of spanwise rotation on the structure of two-dimensional fully developed turbulent channel flow. *J. Fluid Mech.* **56**, 533–557.

Kim, J., Moin, P. & Moser, R. J. 1987 Turbulence statistics in fully developed channel flow at low Reynolds number. *J. Fluid Mech.* **177**, 133–166.

Koyama, H., Masuda, S., Ariga, I. & Watanabe, I. 1979 Stability and destabilizing effects of Coriolis force on two-dimensional laminar and turbulent boundary layers. *Trans. ASME* A: *J. Power Engng* **101**, 23–31.

Kreplin, H. P. & Eckelmann, H. 1979 Behavior of the three fluctuating velocity components in the wall region of a turbulent channel flow. *Phys. Fluids* **22**, 1233–1239.

Kristoffersen, R. & Andersson, H. I. 1993 Direct simulation of low Reynolds number turbulent flow in a rotating channel. *J. Fluid Mech.* **256**, 163–197.

Kristoffersen, R. Nilsen, P. J. & Andersson, H. I. 1990 Validation of Reynolds stress closure for rotating channel flow by means of direct numerical simulations. In *Engineering Turbulence Modelling and Experiments* (ed. Rodi & Ganic), pp. 55–64.

Launder, B. E., Tselepidakis, D. P. & Younis, B. A. 1987 A second-moment closure study of rotating channel flow. *J. Fluid Mech.* **183**, 63–75.

Lezius, D. K. & Johnston, J. P. 1976 Roll-cell instabilities in rotating laminar and turbulent channel flows. *J. Fluid Mech.* **77**, 153–175.

Miyake, Y. & Kajishima, T. 1986 Numerical simulation of the effects of Coriolis force on the structure of turbulence. *Bull. JSME* **29**, 256, 3347–3351.

Nakabayashi, K. & Kitoh, O. 1996 Low Reynolds number fully developed two-dimensional turbulent channel flow with system rotation. *J. Fluid Mech.* **315**, 1–29.

Shima, N. 1993 Prediction of turbulent boundary layers with a second-moment closure: Part II-Effects of streamline curvature and spanwise rotation. *Trans. ASME: J. Fluids Engng* **115**, 64–69.

Watmuff, J. H., Witt. H. T. & Joubert, P. N. 1985 Developing turbulent boundary layers with system rotation. *J. Fluid Mech.* **157**, 405–448.

Wei, T. & Willmarth, W. W. 1989 Reynolds-number effects on the structure of a turbulent channel flow. *J. Fluid Mech.* **204**, 57–95.